*applied sciences*

MDPI

*Article*

# Determination of Heat Transfer Coefficient in a Film Boiling Phase of an Immersion Quenching Process

**Alen Cukrov [1], Yohei Sato [2,3,*], Darko Landek [1], Nikolaus Hannoschöck [4], Ivanka Boras [1] and Bojan Ničeno [2]**

[1] Faculty of Mechanical Engineering and Naval Architecture, University of Zagreb, Ivana Lučića 5, 10002 Zagreb, Croatia; alen.cukrov@fsb.unizg.hr (A.C.); darko.landek@fsb.unizg.hr (D.L.); ivanka.boras@fsb.unizg.hr (I.B.)
[2] Center for Scientific Computing, Theory and Data, Laboratory for Simulation and Modelling, Paul Scherrer Institute (PSI), Forschungsstrasse 111, 5232 Villigen, Switzerland; bojan.niceno@psi.ch
[3] Department of Mechanical and Process Engineering (D-MAVT), ETH Zürich, Leonhardstrasse 21, 8092 Zürich, Switzerland
[4] Independent Researcher, Fohlenstrasse 4, 9472 Grabs, Switzerland; hannoschoeck@sunrise.ch
* Correspondence: yohei.sato@psi.ch

**Abstract:** The numerical solution of flow and temperature fields in and around a hot metal component being immersed into a cooling fluid offers powerful insights into investigating industrial quenching processes. The calculation requires a simultaneous solution of the Navier Stokes and the according energy equation. Difficulties arise at the boundaries where high heat transfer rates are forced from the solid surface to the fluid due to high metal temperatures. Heat transfer rates are determined based on the similarity theory, but reliable heat transfer equations valid for the high temperature typical of quenching processes are rare. This paper presents a two-fluid VOF (volume-of-fluid method) approach, giving an insight into the transient heat transfer and its oscillations. Unlike our previous publications, this paper uses the lumped heat conduction model to obtain the heat transfer coefficient in the film boiling heat transfer mode. Its application leads to an estimation of an average heat transfer coefficient. Furthermore, the unsteady distribution of the heat transfer coefficient values, shown in our previous paper, is now supplemented with the corresponding flow behavior obtained using the numerical simulation. In our approach, the vapor bubble formation during the film boiling phase is tracked directly (DNS of interface motion, not turbulence), and the unsteady heat transfer coefficient distribution is obeyed.

**Keywords:** heat transfer coefficient; film boiling; two-fluid VOF; immersion quenching; bubble evolution; basic principles approach

check for updates

Academic Editors: Bin Yang and Davide Mombelli

Received: 20 November 2024
Revised: 10 January 2025
Accepted: 15 January 2025
Published: 21 January 2025

**Citation:** Cukrov, A.; Sato, Y.; Landek, D.; Hannoschöck, N.; Boras, I.; Ničeno, B. Determination of Heat Transfer Coefficient in a Film Boiling Phase of an Immersion Quenching Process. *Appl. Sci.* **2025**, *15*, 1021. https://doi.org/10.3390/app15031021

**Copyright:** © 2025 by the authors. Licensee MDPI, Basel, Switzerland. This article is an open access article distributed under the terms and conditions of the Creative Commons Attribution (CC BY) license (https://creativecommons.org/licenses/by/4.0/).

## 1. Introduction

One may outline two issues when modeling heat transfer at a real scale. The first is associated with theoretical modeling that requires empirical data in terms of empirical correlations for calculation of the heat transfer coefficient, and the second is the application of numerical simulation software that is, when mass transfer is considered, very expensive in terms of the needed computational resources and time consumption when a fundamental (basic) approach is utilized in obtaining the numerical solution.

To mitigate this, we used a lumped heat conduction model in the estimation of the heat transfer coefficient based on temperature distribution in a material and the corresponding heat conduction time, together with the novel mass transfer model that is used in conjunction with the frozen turbulence modeling approach.

Within the scope of fundamental issues related to the boiling phenomena and correspondingly the associated heat and mass transfer, a single bubble dynamic has been experimentally studied in Barthès [1]. The downward-facing heating element was used to generate the bubble in a subcooled Perfluorhexan liquid (FC-72), and the bubble growth characteristics were examined among other features of the flow in the vicinity of the bubble. Shortly thereafter, the ISO 9950:1995 [2] standard probe made of Inconel 600 nickel alloy was reported in Felde [3]. The oil and water quenchants at different temperature levels were examined using inverse heat transfer analysis (IHTA). Furthermore, at a fundamental research scale, the saturated and subcooled film boiling around a cylinder was studied both theoretically and experimentally in Momoki et al. [4]. The heat transfer surface was partitioned in the bottom, vertical, and top, and by application of different correlations for the calculation of the heat transfer coefficient, the heat flow rate for the entire cylinder was obeyed. The boiling issues related to the immersion quenching process were studied experimentally and numerically (finite element method, FEM) in conjunction with the inverse heat transfer analysis (IHTA) in Demirel [5]. The author used different geometries and different immersion velocities in studying rewetting zones and multipoint sampling of temperature data in the estimation of the heat transfer coefficients via IHTA. The enhanced heat transfer due to the existence of bubbles in the vicinity of the vertical heated surface has been reported within the experimental work described in Donnelly et al. [6]. The noticeable increase in the heat flux was noticed in the presence of the bubbles in contrast to the pure, single-phase, bulk fluid. The heat transfer coefficient during the quenching process was determined by Krause et al. [7]. The authors used a Lee-based mass transfer model in a mixture model formulation, with the dispersed phase being modeled using a bubble crowding approach. The irrelevance of imposing the heat transfer coefficient, as is mandatory in the structural thermal analysis of quenching using IHTA-generated heat transfer coefficient data, is explicitly stated in Kosseifi [8]. The variational multiscale (VMS) approach, which is claimed to be a large eddy simulation (LES) analog within FEM modeling and further explained in John [9], with the well-established level-set method (LS), which is a direct numerical simulation (DNS) of an interface motion (not of turbulence, as clearly noted in Magnini [10]) method known for efficient interface curvature estimation, has been applied in the numerical modeling of the quenching process. Going back to the application of the inverse heat conduction approach, the heat transfer coefficients, together with the cooling rates, were estimated by Landek et al. [11]. The immersion quenching process using water-liquid and polymer-based solutions at different temperature levels has been considered by the authors. As per Tensi [12], the knowledge of rewetting behavior in terms of knowing the rewetting velocity yields an accurate estimation of temperature distribution during the film boiling regime. The rewetting phenomenon may be involved in the simulation via the input of the space-time-dependent heat transfer coefficient in an inverse heat transfer analysis, as noted in Felde and Shi [13]. Furthermore, the application of the heat transfer coefficient in the FEM analysis of the quenching process has been reported in Steuer [14]. The heat transfer coefficients were obtained from the transient temperature distribution in a solid using the finite difference method (FDM). The importance of turbulence kinetic energy in the simulation of the quenching process is outlined in Subhash [15]. The four-equation turbulence model has been used within the framework of numerical modeling of the spray quenching process using AVL Fire computational software (https://www.avl.com/en/simulation-solutions/software-offering/simulation-tools-a-z/avl-fire-m, accessed on 14 January 2025). The already-mentioned VMS approach has been applied in a detailed quenching study of complex geometries in Bahbah [16]. The significance of bubble flow in the enhancement of the heat transfer process has been outlined in the computational study of multiphase flow in Panda [17]. More recently, the

Inconel 600 nickel alloy has been studied from the heat transfer point of view in Ebrahim et al. [18]. The material was considered at a temperature that is lower than the one used in quenching, and the importance of thermal radiation was shown. Finally, the investigation of residual stresses in a Ti6Al4V alloy has been supplemented with combined FEM/CFD simulation methods in a recent study by Gamidi and Pasam [19]. Thus, CFD modeling is utilized for obtaining the heat transfer coefficients, whilst FEM modeling is used for the structural analysis needed for the estimation of residual stresses in the material. In addition, the knowledge of the heat transfer coefficient is viable information in technologies other than quenching, as shown in the recent study by Gupta and Yadav [20]. The authors used CFD techniques to estimate the heat transfer coefficient during the deep grinding process.

Being aware of the dynamic behavior of the heat transfer coefficient during the quenching process, in particular, at the switch between the film and nucleate boiling regimes where a drastic change in heat transfer coefficient takes place, with this paper, we want to further explore this dynamic, but solely in the film boiling phase, where transient oscillations of the heat transfer coefficient also occur.

Thus, by reviewing the work from the past two decades, it is obvious how the bubble dynamics influence on the heat transfer coefficient in the film boiling regime was hard to comprehend via the affordable numerical simulation due to the flow complexity and the associated huge computational resources that are to be used to access the flow behavior at a micro-scale using realistic geometry. Hence, the present work presents the bubble behavior in the film boiling regime at an industrial scale, followed by its impact on the heat transfer coefficient. Furthermore, the issues regarding the accurate estimation of the heat transfer coefficient may be lowered using simple theoretical reasoning.

## 2. Materials and Methods

### 2.1. Analytical Method

Though the Dulong–Petit rule predicts a constant value for the volume specific heat capacity ($\rho \cdot c$) for all solids, where $\rho$ is the solid density and $c$ the specific heat capacity of the solid material, real metals and alloys show individual values that grow with rising temperature. At ambient temperature, 20 °C, ($\rho \cdot c$) = 2.44 MJ/(m$^3$K) for silver and rises (nearly) linearly to 2.73 MJ/(m$^3$K) at 500 °C, as shown in Figure 1. While the density of Inconel is lower than that of silver, its volume specific heat capacity is significantly higher. It grows (nearly) linearly from 3.76 at 20 °C to 4.77 MJ/(m$^3$K) at 600 °C. The heat transfer is hardly influenced by the probe material, and by experience, we expect it to be in the order of 200 to 300 W/(m$^2$K).

Probes of different materials (everything else equal) lead to different $Bi$ numbers according to their different thermal conductivities, as known from the definition of the Biot number [21]. Pure silver shows rather high conductivity. At ambient temperature, that is, $\lambda_{20°C} \approx 430$ W/(mK). The strong condition for a lumped system is $Bi \leq 0.1$, which is, in the case of silver, $h \leq 3558$ W/(m$^2$K). Therefore, a probe of silver and 12 mm diameter will always behave as a lumped system.

The heat conductivity of alloys such as Inconel 600 is more than ten times lower. A typical conductivity at ambient is $\lambda \approx 15$ W/(mK). $Bi \leq 0.1$ leads to $h \leq 124$ W/(m$^2$K). As this boundary is not sharp, we may exceed the limit to $Bi \leq 0.25$, and we may expect nearly lumped conditions for approximately $h \leq 300$ W/(m$^2$K).

Hence, within the scope of the present research, we would apply similar heat transfer coefficient inputs as the starting point in the estimation of the heat transfer coefficient using the lumped heat conduction model.

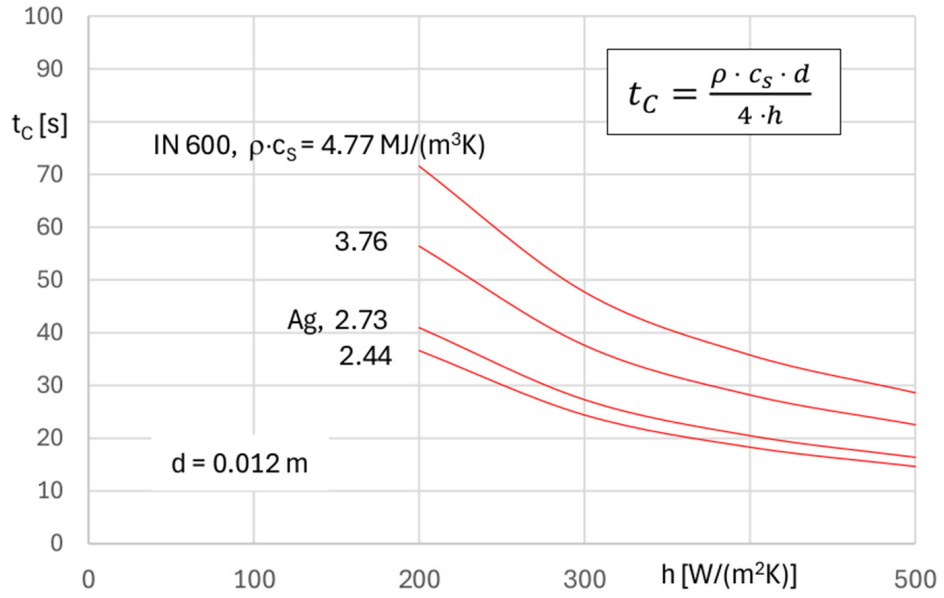



**Figure 1.** Time constant $t_C$ of a cylindrical probe. The volume specific heat capacity ($\rho \cdot c$) is dependent on probe material (Inconel 600 and silver) and temperature, i.e., ambient and 500 °C (silver) and 600 °C (Inconel).

Generally speaking, the heat transfer coefficient could be related to the unsteady temperature distributions using the equation for the determination of the average heat transfer coefficient during the immersion quenching process defined in Bourouga [22] that reads

$$h_{avg} = \frac{1}{(T_{init} - T_b)} \int_{T_{init}}^{T_b} h(T_s) dT_s \quad (1)$$

where $T_{\text{init}}$ is the initial temperature of the specimen, $T_{\text{b}}$ is the bulk fluid temperature, $T_{\text{s}}$ is the specimen's surface temperature, and $h(T_{\text{s}})$ is the heat transfer coefficient's dependence function with respect to the specimen's surface temperature. This function may be determined by inverse analysis from the recorded cooling characteristics using the suitable temperature measuring probe [11,13].

### *2.2. Numerical Method*

#### 2.2.1. Description of the Cases

The goal of this study is to reproduce the real situation during the immersion quenching, i.e., to account for metal immersion (Inconel 600) in obtaining the heat transfer coefficient data. Prior to that step, the cooling of an immersed silver specimen was studied using a numerical method (this may be regarded as immersion with infinite velocity). The schematics of the studied cases with corresponding boundary conditions are shown in Figure 2.

Hence, as an initial point, the cooling of silver specimens with equal diameter and height (45 mm) has been studied (Figure 2c). After the simulation successfully reproduced the experimental results from the literature [4], the final simulation of a realistic probe made of Inconel 600 with the dimensions proposed by the ISO 9950:1995 standard [2], i.e., $D$ = 12.5 mm and $H$ = 60 mm, and with finite immersion velocity (130 mm/s) was studied. Thus, Figure 2a shows the initial configuration in which the probe is 170 mm above the free surface of water, while the final probe position (with the absence of boiling around the specimen surface) is qualitatively displayed in Figure 2b.

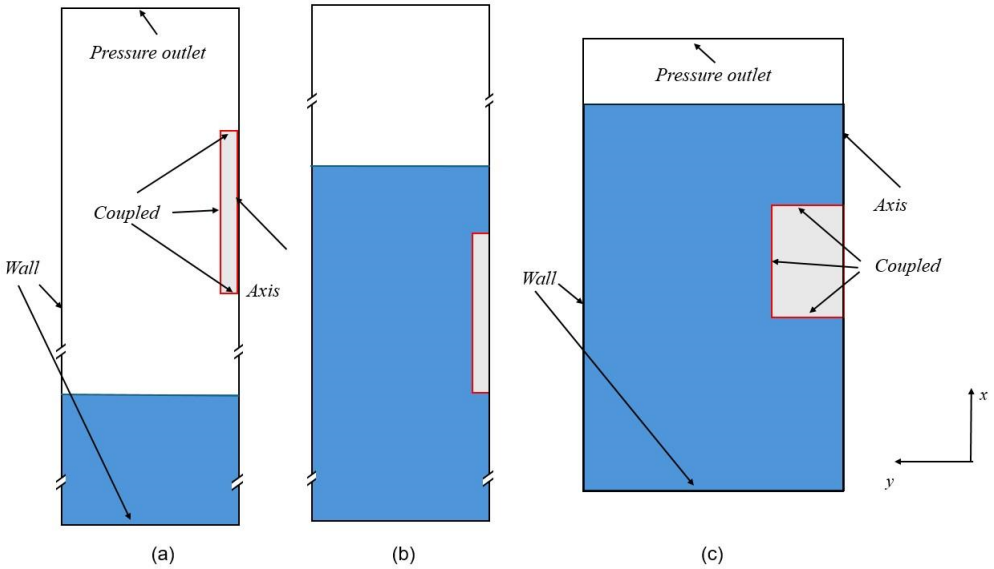



**Figure 2.** The schematic representation of the studied cases. (**a**) The initial setup of Inconel 600 immersion quenching simulation; (**b**) the final position of the probe after immersion; (**c**) the setup for the silver cylinder case.

The independence of the computational grids has been carried out using a one-dimensional Stefan problem, and its detailed description is given in Cukrov et al. [23], with a further discussion in the recent study by Cukrov et al. [24]. It was confirmed that in the case of Eulerian two-fluid modeling, mesh refinement does not play a significant role due to the interphase transfer modeling using constitutive laws. The findings are in accordance with those reported in Gauss et al. [25], where a standard interface tracking case, the rising bubble, was studied using the Eulerian two-fluid model, and the mesh sensitivity was not found to be crucial in obtaining accurate solutions. Furthermore, Liu and Pointer [26] also stress the irrelevance of the application of the fine mesh resolution within the scope of Euler–Eulerian analysis.

#### 2.2.2. General Remarks

The two-fluid VOF model is the most elaborate multiphase flow modeling approach available within the computational software ANSYS Fluent [27], and it is the one capable of handling all types of multiphase flow phenomena [28]. In its derivation, an averaging procedure has been applied [29], and hence, the information regarding the interface position is lost. Consequently, as a product of the averaging procedure, the governing equations include the source terms that are used for modeling the complex interfacial transport, thus making the two-fluid model dependent on closure models that are to be applied within these source terms. Furthermore, in the two-fluid model, each set of conservation equations is solved for each phase that is present in the flow. These equation sets are connected via the already-mentioned source terms that stem from the averaging procedure and that are responsible for interphase transfer. However, since the information about the interface is lost, it is by default not convenient to apply the two-fluid model in separated flows, as, for example, film boiling is. Hence, several attempts were made in the past to mitigate this. The algebraic interfacial area density (AIAD), proposed in Höhne and Vallée [30], and the large bubble model (LBM), used in Denèfle [31], are some of them. In those approaches, as generally known, the interfacial area density, when sharp interface modeling is desired, as needed in the case of separated flow such as in film boiling, is calculated using the volume fraction gradient that reads

$$A_i = |\nabla \alpha_v| \quad (2)$$

where $\alpha$ refers to the volume fraction of the dispersed, in this case, the vapor phase. Thus, the source terms in the governing equation sets are applied locally at the interface between two phases, as graphically outlined in Kharangate et al. [32]. Another approach, according to Mer et al. [33], being on the edge of two-fluid modeling, is the application of the two-fluid model in conjunction with a single fluid LS method, as shown in Štrubelj et al. [34]. Hence, by the application of an extremely high value of the interphase drag, one may obey the behavior of two-fluid modes the same as for a single fluid one since the velocities of both phases are equalized at the interface. This approach has been used in the present work, however, by the application of the two-fluid VOF model, available within the CFD code ANSYS Fluent [27]. The details regarding the method applied herein are given in detail in Cukrov et al. [23].

#### 2.2.3. Mathematical Model

The mathematical model that governs the studied phenomenon has already been presented in Cukrov et al. [23] and will be briefly examined herein. The concept of interpenetrating continua relies on the fact that each phase occupies the whole domain, and thus, a separate set of conservation equations is solved for each phase. In the present case, written for $q$-th phase, which could be either vapor or liquid, we have

- conservation of mass:

$$\frac{\partial}{\partial t}(\alpha_q \rho_q) + \nabla \cdot \left(\alpha_q \rho_q \vec{v}_q\right) = \dot{m}_{pq} \tag{3}$$

- conservation of momentum:

$$\frac{\partial}{\partial t}\left(\alpha_q \rho_q \vec{v}_q\right) + \nabla \cdot \left(\alpha_q \rho_q \vec{v}_q \vec{v}_q\right) = -\alpha_q \nabla p + \nabla \cdot \bar{\bar{\tau}}_q + \vec{R}_{pq} + \dot{m}_{pq} \vec{v}_{pq} \tag{4}$$

- conservation of energy:

$$\frac{\partial}{\partial t}(\alpha_q \rho_q h_q) + \nabla \cdot \left(\alpha_q \rho_q \vec{u}_q h_q\right) = \alpha_q \frac{dp_q}{dt} + \bar{\bar{\tau}}_q : \nabla \vec{u}_q + \Phi_{pq} + \dot{m}_{pq} r_0 \tag{5}$$

where $\alpha_q$ denotes the volume fraction of $q$-th phase, $\rho_q$ is $q$-th phase's density, $\vec{v}_q$ is the $q$-th phase velocity, $\dot{m}_{pq}$ is the mass transfer rate per unit volume for a phase pair, $p$ is the system pressure, $\bar{\bar{\tau}}_q$ is the $q$-th phase stress-strain tensor, $\vec{R}_{pq}$ is the general representative of the interphase drag, $\vec{v}_{pq}$ is the interphase velocity, $h_q$ is $q$-th phase specific enthalpy, $\Phi_{pq}$ is the interphase heat transfer term, and $h_{pq}$ is the specific heat of vaporization. The derivation of the mass transfer model applied herein is presented in the Appendix A.

Additionally, as noted by Lopez de Bertodano et al. [35], the two-fluid model stems from Landau's Nobel theory for the superfluidity of Helium. The author, furthermore, brings out the concise historical development of the two-fluid model, thereby addressing its stability problem. Apart from its classical application within nuclear and chemical engineering, it is also a promising approach to resolving turbulent motion [36], which, to the author's knowledge, is a last and, until now, unresolved problem of classical physics.

#### 2.2.4. Boundary Conditions

The incorporated concept of interpenetrating continuum, which has already been mentioned in the previous subsection, also requires the prescription of boundary conditions on a per-phase basis. The schematics of the applied boundary conditions are shown in Figure 2 and will be briefly covered in what follows.

A two-dimensional axisymmetric domain has been chosen, with an $x$-axis as the symmetry axis due to software requirements. The Dirichlet boundary condition has been applied at the top of the domain by the prescription of the vapor volume fraction of the bulk fluid temperature.

The "coupled" boundary condition available within ANSYS Fluent has been used at the solid–fluid boundary in order to establish the communication between the energy equations in the fluid part of the domain and the transient heat conduction equation in the solid part. All the other walls that were present in the flow were treated as adiabatic ones.

#### 2.2.5. Mass Transfer Modeling

Originating from continuum mechanics, the energy jump model is based on heat flux balance at the phase interface, which, in turn, yields mass transfer across it. Among the other well-established approaches is the Lee and Schrage model, together with the energy jump model summarized by Kharangate and Mudawar [37]; this approach does not require the application of empirical parameters for its application due to its basic principle's foundations. However, an initial vapor layer must be prescribed in order to induce mass transfer across the interface. Within the scope of the present research, a model that stems from the balance between the energy jump and the thermal phase change model, which is proposed by Cukrov et al. [23], is used.

#### 2.2.6. Turbulence Modeling

The laminar flow model, in conjunction with the mass transfer model proposed herein, would not yield the accurate extraction of the heat flow rate from a specimen. Hence, a turbulence model, that is, the turbulent viscosity, needs to be addressed to this end. In doing so, due to complexities related to the application of turbulence modeling in such a case (high temperatures and high heat flow rates), we chose a frozen turbulence modeling approach that is extensively described by Cukrov et al. [38]. The model is based on the prescription of the turbulent kinetic energy value through the domain, and this value has been determined parametrically. Furthermore, it was found that the value of turbulent kinetic energy may be accurately tracked by the application of the Kelvin–Helmholtz instability theory approach proposed by Hillier et al. [39] in conjunction with the boundary layer analysis outputs proposed by Yamada et al. [40].

#### 2.2.7. Mesh Motion

Due to the motion of the specimen made of Inconel 600 nickel alloy, one needs to ensure the appropriate technique for the establishment of accurate mesh motion. Within the present research, it is done by the application of the arbitrary Lagrangian–Eulerian (ALE) method, in which the two domains (solid and fluid) are distinguished by a solid boundary that is explicitly tracked (Lagrangian approach), while within each domain, the equations are being solved in a Eulerian, control volume approach. The mathematical outline of the ALE method is available in Aubram [41]. Since the motion of a specimen is by far more than just an oscillation of, for example, a droplet in a zero-gravity area, it is necessary to use the remeshing method to overcome the huge displacements that are to appear when a body is moving from its initial point toward the quenchant liquid. The applied method herein is briefly described, together with other numerical simulation features, in Cukrov et al. [42]. The remeshing problem has been tackled by Dobrzynski [43], while its application within the ALE solver is shown by Olivier [44] and Barral [45].

2.2.8. Integral Quantities Calculation: Heat Fluxes and Heat Transfer Coefficients

The wall heat flux and the wall temperature may stem from the following reasoning. Let the temperatures of fluid, $T_{\text{fluid}}$, and solid, $T_{\text{solid}}$, in a system shown in Figure 3 be known and, in addition, the local thermal equilibrium may be assumed.

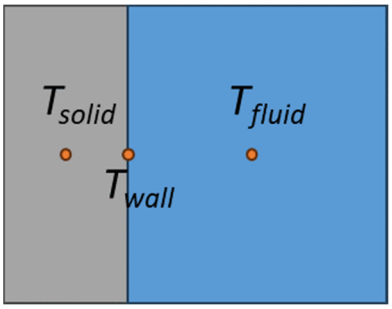



**Figure 3.** The wall adjacent system in a conjugate heat transfer case.

Therefore, we can write the heat fluxes at each side of the solid wall as follows:

$$q_s = \lambda_s \frac{(T_{wall} - T_{solid})}{\Delta x_{solid}} \tag{6}$$

$$q_s = \lambda_f \frac{\left(T_{fluid} - T_{wall}\right)}{\Delta x_{fluid}} \tag{7}$$

From these two equations, Equations (6) and (7), one may obey the wall heat flux, $q_s$, and the wall temperature, $T_{\text{wall}}$.

By further exploration of Equation (7), one may note the necessity for the definition of effective thermal conductivity in the case of turbulent flow, that is, that the thermal conductivity at the liquid side is actually a sum of molecular and turbulent thermal conductivities, $\lambda_f = \lambda_m + \lambda_t$. In doing so, the molecular thermal conductivity refers to the physical property of the fluid, and it is the only one considered in the laminar flow, while the turbulent thermal conductivity (present if the flow is turbulent) is the flow dependent variable and could be estimated using either the turbulent viscosity via the turbulent Prandtl number or the wall function.

The heat transfer coefficient, on the other hand, is defined as the ratio between the wall heat flux and the temperature difference between the solid surface and the bulk fluid, as follows:

$$h = \frac{q_s}{T_{wall} - T_\infty} \tag{8}$$

where $q_s$ is the wall heat flux, $T_{\text{wall}}$ is the wall temperature, and $T_\infty$ is the bulk fluid temperature. Within the scope of the present work, an area weighted average heat transfer coefficient has been taken into consideration within the discussion of the results, as follows:

$$\underline{h} = \int_A h dA \tag{9}$$

The average heat transfer data has been computed within postprocessing of the results and presented herein for the overall heat transfer surface in the case of silver specimens and partitioned only for a vertical surface of the cylinder in the case of the Inconel 600 superalloy since the dominant heat transfer is to appear on this heat transfer surface. The overbar in Equation (9) will be omitted in further discussions of average heat transfer coefficients in this paper.

### 2.3. Studied Materials

#### 2.3.1. Silver

The silver probe with constant thermal properties has been analyzed in this study. The details regarding the studied probe with dimensions $D = H = 45$ mm and the experimental apparatus used in the determination of the temperature distribution, which is necessary for the calculation of the time constant in the lumped heat conduction model in its center, are given in Momoki et al. [4]. On the other hand, the details regarding the numerical computation of the film boiling with the accompanied conduction heat transfer in the silver specimen (conjugate heat transfer problem) using the two-fluid VOF model were explained in Cukrov et al. [38].

The material has no allotropic modifications and is preferred for heat treatment estimates in Japan [46]. Furthermore, the material is suitable for an analysis using the lumped heat conduction model due to the small Biot number, i.e., within the present study, the Biot number is 0.02, an order of magnitude less than the limiting 0.1 value. In the determination of the Biot number in the present case, the following data have been used from the material properties table given in Hannoschöck [21]. The thermal conductivity is 421 W/(m K), the material density is 10,490 kg/m$^3$, and the specific heat capacity is 234 J/(kg K). This very low Biot number is calculated by an assumption that the heat transfer coefficient is 400 W/(m$^2$ K). The material effusivity, calculated as $b = \sqrt{\lambda_s \rho c_p}$, is high enough that the standard, expectable boiling modes are present in the flow and is 32,146 Ws$^{0.5}$/(m K). The relevance of thermal effusivity for the occurrence of standard boiling modes is noted in Jagga and Vanapalli [47].

#### 2.3.2. Inconel 600

Due to the high temperature sensitivity of the material properties of the nickel alloy Inconel 600, that is, according to ISO 9950 standard ($D = 12.5$ mm; $H = 60$ mm), a mandatory material that is used in the determination of the quenching power of quenchant liquids, the temperature change in thermal conductivity, and the specific heat capacity need to be taken into consideration in the present study. According to the data on thermal conductivities with respect to the temperature given in Hannoschöck [21], one may obey the polynomial distribution of thermal conductivity as follows:

$$\lambda_s(T) = AT^3 + BT^2 + CT + D \tag{10}$$

where the constants are $A = 1.34 \times 10^{-10}$ W/(m K$^4$); $B = 2.75 \times 10^{-6}$ W/(m K$^3$); $C = 1.24 \times 10^{-2}$ W/(m K$^2$); and $D = 1.09 \times 10^{1}$ W/(m K). Integrating Equation (10) in the temperature limits $T_1$ and $T_2$, and division by the temperature difference $\Delta T = T_2 - T_1$ yields an average thermal conductivity within the desired temperature range that reads

$$\lambda_m = [\lambda_s]_{T_1}^{T_2} = \frac{1}{\Delta T}\int_{T_1}^{T_2} \lambda_s(T)dT = \frac{\frac{A}{4}\left(T_2^4 - T_1^4\right) + \frac{B}{3}\left(T_2^3 - T_1^3\right) + \frac{C}{2}\left(T_2^2 - T_1^2\right) + D(T_2 - T_1)}{T_2 - T_1} \tag{11}$$

This value is used in the lumped heat conduction model applied herein and reads 21 W/(m K) for the temperature range 959.3 to 1123.1 K, that is, from 686.2 to 849.9 °C.

Furthermore, in the direct estimation of the heat transfer coefficient using the lumped heat conduction model, it is necessary to provide the average specific heat capacity of the solid material. Due to its strong temperature dependence, a polynomial distribution of the specific heat capacity is found and reads

$$c_s(T) = AT^4 + BT^3 + CT^2 + DT + E \tag{12}$$

where the constants are $A = -1.42 \times 10^{-9}$ J/(kg K$^5$); $B = 4.13 \times 10^{-6}$ J/(kg K$^4$); $C = -4.25 \times 10^{-3}$ J/(kg K$^3$); $D = 2.02$ J/(kg K$^2$); and $E = 1.14 \times 10^2$ J/(kg K). The average specific heat capacity is thus

$$c_{s,m} = \frac{1}{\Delta T}\int_{T_1}^{T_2} c_s(T)dT = \frac{\frac{A}{4}\left(T_2^4 - T_1^4\right) + \frac{B}{3}\left(T_2^3 - T_1^3\right) + \frac{C}{2}\left(T_2^2 - T_1^2\right) + D(T_2 - T_1)}{T_2 - T_1} \quad (13)$$

In this case, the obtained average specific heat capacity for Inconel 600 is 610.3 J/(kg K) in the temperature range $T \in$ [849.90, 686.18] °C = [1123.05, 959.33] K.

Assuming the heat transfer coefficient of value 500 W/(m$^2$ K), and by applying the average thermal conductivity calculated using Equation (11), one may obtain the value of the Biot number equal to 0.149, which is on the edge of the aforementioned criterion 0.1 but still in the frame of thermodynamically thin material. Therefore, for the sake of simplicity, the lumped heat conduction model will be applied herein in the determination of the heat transfer coefficient for the selected time of the quenching process. It is, however, known that since it is derived under the assumption that there are no temperature gradients with respect to space in a solid body, the lumped heat conduction model may be applied in the center of the solid, where the temperature gradients are the smallest in value.

The material density is taken as a constant value, $\rho_s = 8470$ kg/m$^3$. The thermal effusivity is depicted in Figure 4 using the temperature-dependent thermal conductivity and specific heat capacity according to Equations (10) and (12).

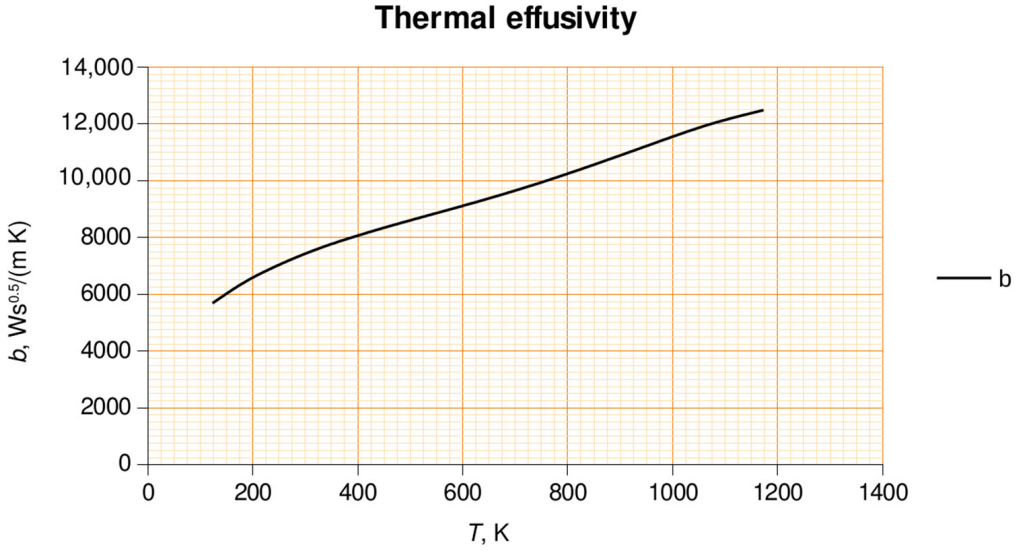



**Figure 4.** Thermal effusivity of Inconel 600 with respect to temperature.

The relatively high values of the thermal effusivity indicate the standard boiling modes would occur during the cooling of a high-temperature object made of this material. The thermal diffusivity, defined as $a_s(T) = \lambda_s(T)/[\rho_s \cdot c_s(T)]$, on the other hand, follows the pattern depicted below in Figure 5 and is computed using Equations (10) and (12), together with a constant density input.

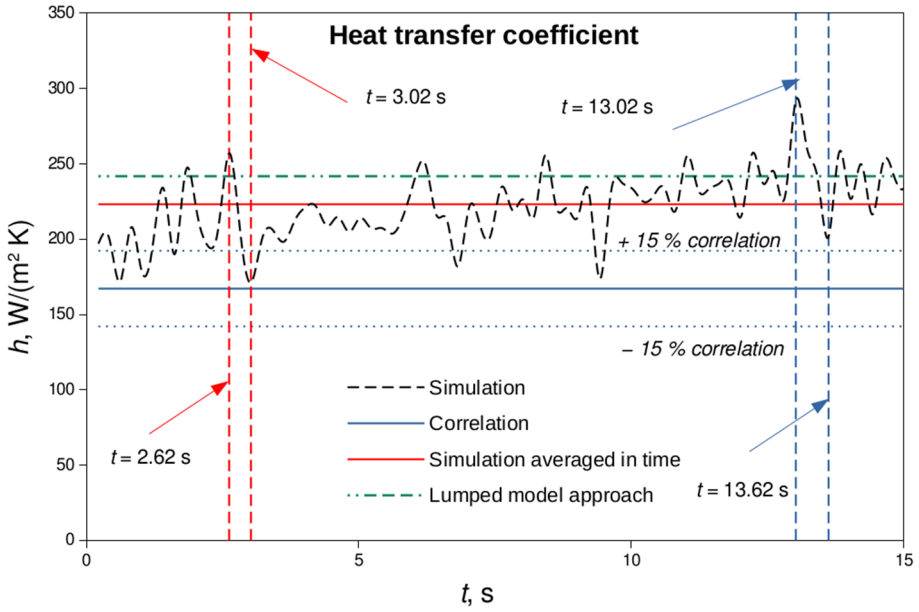



**Figure 5.** Thermal diffusivity of Inconel 600 with respect to the material temperature.

## 3. Results

### *3.1. Silver Specimen*

The transient oscillations in heat transfer coefficient due to complex bubble motion are shown in Figure 6. This plot, however, without a lumped model and the outlined time instances, has been shown in [38]. Hence, in this paper, new insights on the obtained results with the proposed numerical method are made, accompanied by the lumped heat conduction estimate.

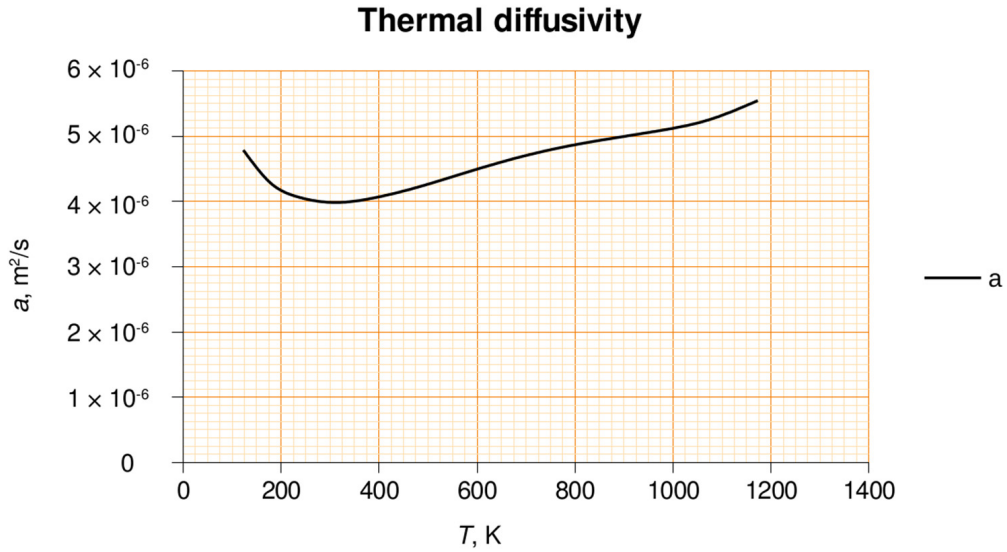



**Figure 6.** Comparison of the heat transfer coefficient calculated using different approaches. The vertical long dash lines denote the time instances with observable bubble detachments (maximum heat transfer coefficient values) and continuous vapor, i.e., dry zones.

At $t$ = 0 s, the specimen is immersed in the cooling water and has been kept through the simulation at the place. The initial simulation time has been shifted for a time increment due to the presence of an initial vapor layer. The dashed line shows the distribution of the heat transfer coefficient at the outer surface of the cylinder specimen derived by the simulation. The transient oscillations in the heat transfer coefficient could be explained by

the intermittent occurrence of dry spots, i.e., the areas where the heat transfer surface is not being wetted by the surrounding liquid, and hence, the heat transfer is less active. The red solid line indicates the time-averaged simulation result, yielding a conclusion that slightly overestimates the error band associated with the correlation data used in the investigation. For plausibility, we added the heat transfer coefficient (green dash dotted line) derived with the lumped heat conduction model for the simulated temperature in the center of the specimen at $t = 0$ and $t = 15$ s.

As shown in Barthès [1], the bubble detachment and dry areas are causing local maximums and minimums in the heat flux distribution, respectively; the tendency is evident within the present research, as shown in Figure 6. In this case, the global minimum is reported at $t = 3.0$ and reads $h = 171$ W/(m$^2$ K), whilst the global maximum is noted at the time instance $t = 13.0$ s with $h = 292$ W/(m$^2$ K). Both extrema with their neighborhood counterparts were denoted in Figure 6 and further examined herein.

The vapor bubble is generated after enough heat is transferred to a layer in the vicinity of the heated surface. The bubble formation and its interaction with the surroundings is described in Mayinger [48]. The bubbles are generated at the so-called nucleation sites, whose number also depends on the heat flux at the heated surface. Once generated, the bubble receives the heat input from the bulk liquid since the liquid is in a meta-stable superheated state and evaporates at the interface between the vapor and liquid. Thus, the vapor bubble grows and, at a certain time instance, detaches from the nucleation site with the frequency of detachment that depends on the heat load imposed at the bottom surface.

After the disbalance in forces acting on the bubble, according to the theoretical exposure in Bucci et al. [49], the bubble departs, the vapor bubble rises, liquid flows afterwards to re-fill the vapor volume, and finally, the vapor bubble reaches the free surface of the liquid and causes the instability of the free surface of the liquid.

Referring to the left part of the heat transfer coefficient distribution (dashed red line), the peak in the heat transfer coefficient coincides with the detached bubble at the top horizontal surface of a specimen, as shown in Figure 7a. Also, the minimum value (local minimum) is found at a point where continuous vapor film is present from the horizontal surface of the specimen to the free surface level, as shown in Figure 7b.

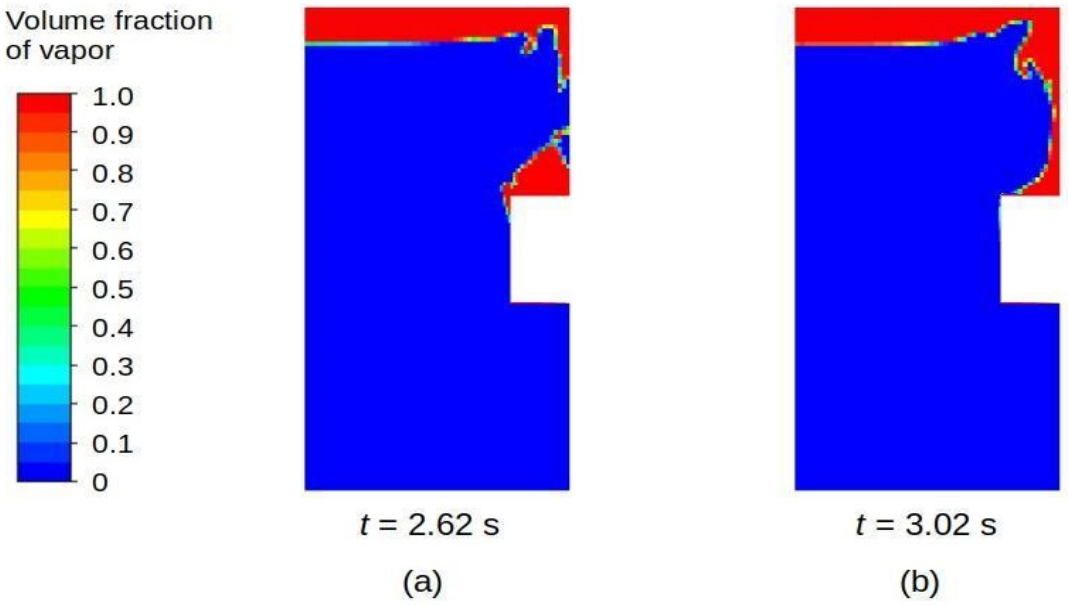



**Figure 7.** (**a**) Bubble detachment; (**b**) a continuous vapor zone between the free surface of the liquid and the top horizontal surface of the specimen. The selected time instances are $t = 2.62$ s and $t = 3.02$ s. Blue is liquid; red is the vapor zone.

On the other hand, looking at the right part in Figure 6 (dashed blue line), i.e., at the global maximum of the heat transfer coefficient, it is hard to comprehend the direct relation between the vapor volume fraction distribution in the domain and the heat transfer coefficient value, judging by the field distribution of the vapor volume fraction in Figure 8. Hence, further investigation is needed to obtain adequate conclusions on this point.

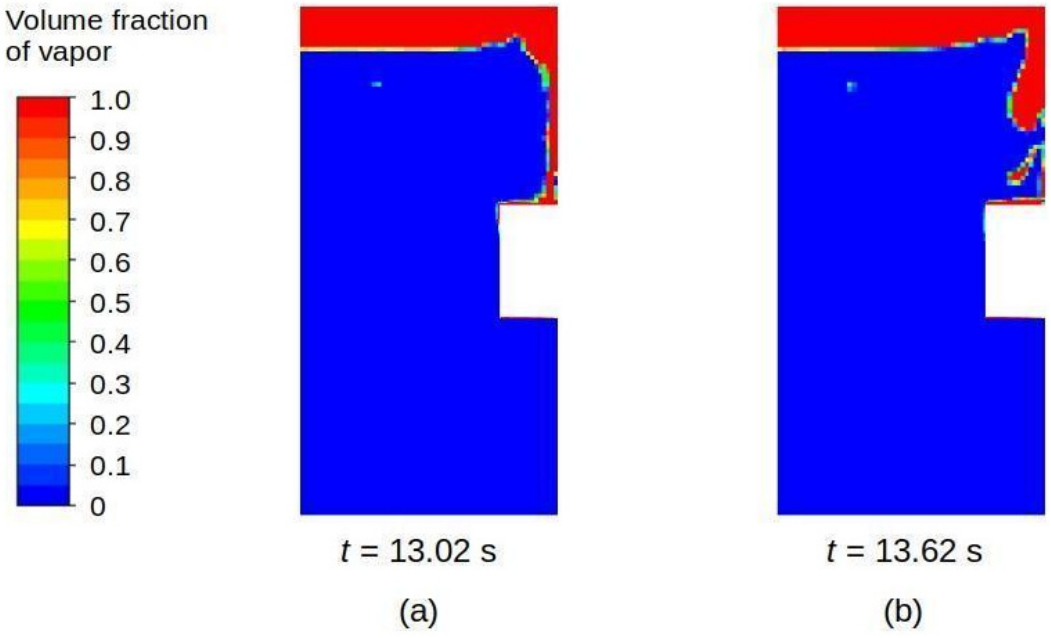



**Figure 8.** (**a**) Vapor phase flow patterns at the global maximum in the heat transfer coefficient shown in Figure 5, that is, at $t$ = 13.02 s; (**b**) the breakup of the continuous vapor zone at $t$ = 13.62 s.

The lumped heat conduction model estimation of the heat transfer coefficient has been found to closely follow the time-averaged simulation data, as denoted by the green line in Figure 6. The input data are as follows: In the characteristic time of the lumped heat conduction model, the total time is set to 15 s, which corresponds to the period of the experiment by Momoki et al. [4] that is supplemented with the available simulation data in [38]. The temperatures were set to $T(t = 15\ \text{s}) = 812.6$ K (538.5 °C); $T_\infty = 373.15$ K (100 °C); and $T_0 = 873.15$ K (600 °C).

Thus, the thermal time constant of 114.2 s is obtained. Using this value, one obeys the heat transfer coefficient of value 242 W/(m$^2$ K), which is included in Figure 6. It was shown that a detailed numerical simulation using a two-fluid VOF model yields a slightly lower time-averaged result, i.e., $h$ = 223 W/(m$^2$ K), or 7.7% is the discrepancy between the analytical and the time-averaged simulation result.

### *3.2. Inconel 600 Specimen*

Regarding the data related to the heat transfer analysis of the Inconel 600 nickel alloy, part of these results is available in Cukrov et al. [24], while the overall heat flow rate, together with the temperature distribution comparison with two sources, may be found in [50]. However, neither publication includes the contribution of the lumped heat conduction model, as shown in Figure 9.

Since the application of the IHTA method, which is demonstrated in Landek et al. [11], refers to the local measuring point area, the data obtained using this method would be regarded as for the vertical surface of a cylinder. Hence, all the estimates would be referred to ones that are valid for this heat transfer surface of the material.

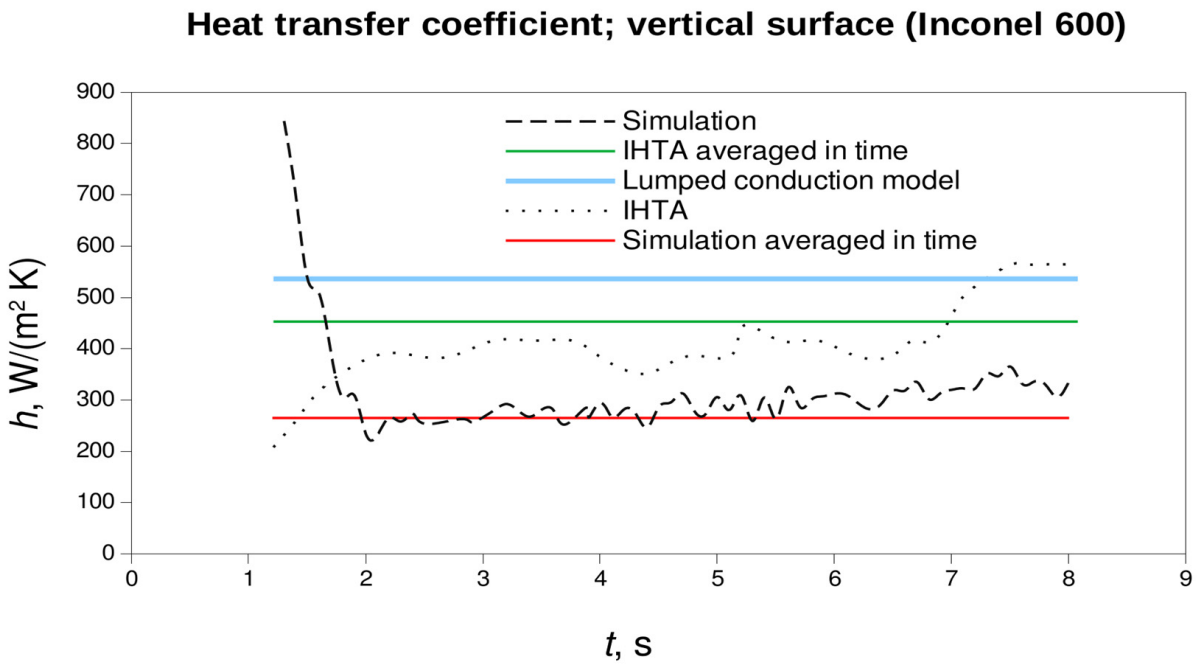



**Figure 9.** The transient distribution of the heat transfer coefficient for the vertical surface of Inconel 600 nickel alloy. The joint comparison between different estimation approaches.

The application of the lumped heat conduction model yields the value of the heat transfer coefficient of 536 W/(m$^2$ K) using the following input parameters: the temperature at which the measurement system starts recording is $T_0$ = 1123.05 K (849.9 °C); the temperature at the end time of the performed numerical simulation in [42] is $T(t = 8\ \text{s})$ = 959.33 K (686.2 °C); and the ambient temperature is taken from the experiment in [11], $T_\infty$ = 333.15 K (60 °C). Thus, the time constant is $t_C$ = 30.1 s, while from Equation (13), one obtains the temperature-averaged specific heat capacity of 610.3 J/(kg K).

The discrepancy from the IHTA method is thus found to be 18.4%, whilst the disagreement of the numerical simulation with the IHTA method is 41.5%. According to Yamada et al. [40], the discrepancies of ca. 30% are regarded as reasonably well. The simulation result, however, might be further enhanced by the modification of the turbulent kinetic energy in the applied frozen turbulence model. Since the intention of this research is to rely mostly on the basic principles approach, fine-tuning any variable is found to be inappropriate.

## 4. Conclusions

The application of an industrially feasible computational model within the context of heat transfer coefficient determination in an industrially relevant metal quenching process has been presented in this paper. The proposed approach includes two-fluid VOF modeling of the film boiling process using the appropriate closures; the mass transfer model that stems from the balance between the energy jump that relates the mass transfer across the interface with the temperature gradient of an unsaturated phase at the interface; the thermal phase change model; and the lumped heat conduction model for the estimation of transient thermal characteristics in a solid material. From the exposure given in the present research, the following conclusions may be drawn:

1. Using the already available features of the anisotropic drag model and the zero-resistance and thermal phase change model, a novel mass transfer model has been successfully included within the ANSYS Fluent computational package. The model is

included in software via the user-defined functions (UDFs), and the main idea behind model implementation is summarized in the Appendix A.

2. The novel method improves the simulations by making it possible to conduct complex boiling computations on a real geometry with real physical properties using moderate computational resources. Furthermore, the empiricism that was associated with the two-fluid model is alleviated by using the two-fluid VOF model in conjunction with the novel mass transfer model and the appropriate closures already available within the ANSYS Fluent.
3. It was found, at the beginning of the film boiling process, that the bubble collapse yields a peak in the heat transfer coefficient, while the dry zone leads to the local minimum of the heat transfer coefficient (global minimum).
4. However, it was not clear at a later stage whether the same finding noted for the second item could be applied, and additional effort is needed in this regard to distinguish the reason for the global maximum and the following local minimum in the heat transfer coefficient.
5. The proposed lumped heat conduction model that stems from basic principles, i.e., by equalization of the first law of thermodynamics and Newton's cooling law, was found to be an efficient tool in the estimation of the heat transfer coefficient when the unsteady temperature distribution is known and the time constant could be determined.

**Author Contributions:** Conceptualization, A.C. and D.L.; methodology, A.C., Y.S. and N.H.; software, Y.S. and I.B.; validation, A.C. and D.L.; formal analysis, A.C., D.L. and I.B.; investigation, A.C. and D.L.; resources, D.L. and I.B.; data curation, D.L.; writing—original draft preparation, A.C. and N.H.; writing—review and editing, D.L., Y.S. and N.H.; visualization, A.C.; supervision, D.L., Y.S. and I.B.; project administration, B.N.; funding acquisition, I.B. and B.N. All authors have read and agreed to the published version of the manuscript.

**Funding:** This research received no external funding.

**Institutional Review Board Statement:** Not applicable.

**Informed Consent Statement:** Not applicable.

**Data Availability Statement:** The data presented in this study are available on request from the corresponding author. The data are not publicly available due to privacy restrictions.

**Acknowledgments:** The useful insights and comments from Antun Galović are gratefully acknowledged and applied in the paper. Furthermore, the first author would like to express his appreciation to Željko Tuković for an insightful discussion on temperature gradient at the fluid part of the liquid–solid interface.

**Conflicts of Interest:** The authors declare no conflicts of interest.

## Nomenclature

**Latin symbols**

| Quantity | Description | Unit |
|---|---|---|
| $A_\mathrm{i}$ | interfacial area density/concentration | $\mathrm{m}^{-1}$ |
| $a_\mathrm{s}$ | the thermal diffusivity of the solid | $\mathrm{m}^2/\mathrm{s}$ |
| $b$ | thermal effusivity | $\mathrm{Ws}^{0.5}/(\mathrm{m\ K})$ |
| $c_\mathrm{s}$ | the specific heat capacity of a solid | J/(kg K) |
| $C_v$ | vapor phase's scaling factor in the thermal phase change model | 1 |
| $D$ | the diameter | m |
| $d_v$ | the vapor phase's diameter | m |
| $g$ | gravitational acceleration | $\mathrm{m}/\mathrm{s}^2$ |

| | | |
|---|---|---|
| $\nabla\alpha$ | gradient of the volume fraction field | $m^{-1}$ |
| $h$ | the heat transfer coefficient | $W/(m^2\ K)$ |
| $h_{pq}$ | interphase heat transfer coefficient | $W/(m^2\ K)$ |
| $H$ | height of a specimen | m |
| $\ddot{m}_{pq}$ | mass transfer rate per unit volume for a phase pair | $kg/(s\ m^3)$ |
| $\vec{n}$ | normal vector | m |
| $p$ | system pressure | Pa |
| $q_l$ | heat flux from liquid to the interface | $W/m^2$ |
| $q_s$ | heat flux at the solid wall | $W/m^2$ |
| $q_v$ | heat flux from vapor phase to the interface | $W/m^2$ |
| $r_0$ | specific heat of vaporization | J/kg |
| $\vec{R}_{pq}$ | general representative of the interface drag term | $kg/(m^2\ s^2)$ |
| $S_e$ | heat flux at the interface (source term) | $W/m^2$ |
| $T$ | thermodynamic (absolute) temperature in degrees Kelvin | K |
| $t$ | time | s |
| $T_{sat}$ | saturation temperature | K |
| $T_{silid}$ | solid temperature | K |
| $T_\infty$ | the free stream temperature | K |
| $TKE$ | turbulent kinetic energy (specific) | $m^2/s^2$ |
| $T_l$ | liquid phase's temperature | K |
| $T_v$ | the temperature of the vapor phase | K |
| $T_w$, $T_{wall}$ | the wall temperature | K |
| $u_p$ | $p$-th phase velocity | m/s |
| $V_c$ | cell volume | $m^3$ |
| $V_{c,i}$ | the volume of $i$-th cell | $m^3$ |
| $\vec{v}_q$ | the velocity of the phase $q$ (either vapor or liquid) | m/s |
| $w$ | flow velocity | m/s |
| $x$ | spatial coordinate | m |

**Greek letters**

| Quantity | Description | Unit |
|---|---|---|
| $\alpha_l$ | the volume fraction of a liquid phase | 1 |
| $\alpha_v$ | the vapor volume fraction | 1 |
| $\lambda$ | molecular thermal conductivity of a material | W/(m K) |
| $\lambda_{eff}$ | effective thermal conductivity | W/(m K) |
| $\lambda_m$ | average thermal conductivity of a solid material | W/(m K) |
| $\lambda_s$ | thermal conductivity of a solid material | W/(m K) |
| $\lambda_t$ | turbulent thermal conductivity | W/(m K) |
| $\lambda_{vap}$ | thermal conductivity of a vapor phase | W/(m K) |
| $\mu_v$ | the dynamic viscosity of a vapor phase | Pa s |
| $\nu_v$ | the kinematic viscosity of a vapor phase | $m^2/s$ |
| $\rho$ | density | $kg/m^3$ |
| $\rho_s$ | the density of the solid | $kg/m^3$ |
| $\rho_q$ | density of $q$-th phase | $kg/m^3$ |
| $\sigma$ | surface tension | N/m |
| $\Phi_{pq}$ | the heat flow rate from the interface to the liquid phase in a vapor–liquid phase change process | $W/m^3$ |

## Appendix A

Let us consider the planar vapor–liquid interface in a phase change process, as shown in Cukrov et al. [23]. In addition, let us consider the most general industrial case in which the flow is turbulent, and the molecular thermal conductivity would be appended with the turbulent thermal conductivity in energy balance at the vapor–liquid interface, as demonstrated in Sato and Ničeno [51]. Assuming that the ratio between the interfacial area and the cell volume is equal to the magnitude of a gradient of a volume fraction, the energy balance at the interface would read

$$\dot{m}_{pq} r_0 = \left\{ (\lambda_l + \lambda_t)(\nabla T_l) \cdot \vec{n} + \left[ -(\lambda_v + \lambda_t)(\nabla T_v) \cdot \vec{n} \right] \right\} |\nabla \alpha_v| \tag{A1}$$

By further assumption of laminar flow and the saturated liquid, the above equation, when divided by the specific heat of vaporization, reduces to

$$\dot{m}_{pq} = \frac{\left[ -\lambda_v (\nabla T_v) \cdot \vec{n} \right] |\nabla \alpha_v|}{r_0} \tag{A2}$$

On the other hand, in the thermal phase change model, the convective heat transfer at the interface is introduced, as shown in [27], and the equation for the mass transfer at the interface in the case of saturated liquid ($T' - T_{\text{liq}} = 0$) would read

$$\dot{m}_{pq} = -\frac{C_v h_v |\nabla \alpha_v| (T_{sat} - T_v)}{r_0} \tag{A3}$$

where the calibration factor $C_v$ is equal unity because we want to keep the basic principles in the mass transfer modeling, thereby avoiding any fine-tuning of model parameters.

By the equalization of Equations (A2) and (A3), and by further assuming that the distance between the interface and neighboring cell's center is half the width of the computational cell, that is, $dx = \Delta x/2$, and that the temperature gradient projection may be approximated as $\nabla T_v \cdot \vec{n} = (T_{sat} - T_v)/dx = 2(T_{sat} - T_v)/\Delta x$, we have the interphase heat transfer coefficient that reads

$$h_v = \frac{2\lambda_v}{\Delta x} \tag{A4}$$

Bearing in mind that the interfacial heat transfer coefficient is defined as

$$h_v = \frac{\lambda_v Nu_v}{d_v} \tag{A5}$$

We arrive at the expression for the Nusselt number, which has only a fictitious function since it is used to actually approximate the temperature gradient in the interface region, as follows:

$$Nu_v = \frac{2d_v}{\Delta x} \tag{A6}$$

The vapor phase diameter, dv, that is present in Equation (A6) is the value that is manually inserted into the software. But, due to the heat transfer coefficient definition, e.g., Equation (A5), this quantity vanishes, and the resulting heat transfer coefficient is defined with Equation (A4).

The model is implemented within ANSYS Fluent as a UDF in the context of interphase models via the Define-Exchange-Property macro. Equation (A6) is thus subjected to the procedure for the calculation of the heat transfer coefficient, and this value has been returned by the Define-Exchange-Property macro.

Furthermore, it is important to note that, prior to computation, the initial flow fields need to be initialized using the Define-Init macro on a per-phase basis. Hence, due to the interpenetrating continua concept that underlies the two-fluid modeling, one should access all the fields and, in each of them, prescribe the initial values of volume fraction, velocity components in x- and y-directions, fluid temperature, and the turbulent kinetic energy, since the flow is turbulent and the frozen turbulence approach has been used in the study.

## References


1. Barthès, M. Ebullition Sur Site Isolé: Étude Expérimentale de la Dynamique de Croissance d'une Bulle et des Transferts Associés. Ph.D. Thesis, Université de Provence—Aix-Marseille I, Marseille, France, 2005.
2. *ISO 9950:1995*; Industrial Quenching Oils—Determination of Cooling Characteristics—Nickel-Alloy Probe Test Method. International Organization for Standardization: Geneva, Switzerland, 1995.
3. Felde, I. Új Módszer Acélok Edzéséhez Használatos Hűtőközegek Hűtőképességének Minősítésére. Ph.D. Thesis, Miskolci Egyetem, Műszaki Anyagtudományi Kar, Kerpely Antal Anyagtudományok és technológiák Doktori Iskola, Miskolc, Hungary, 2007.
4. Momoki, S.; Yamada, T.; Shigechi, T.; Kanemaru, K.; Yamaguchi, T. Film Boiling Around a Vertical Cylinder With Top and Bottom Horizontal Surfaces. In Proceedings of the HT2007; ASME/JSME 2007 Thermal Engineering Heat Transfer Summer Conference, Vancouver, BC, Canada, 8 July 2007; Volume 2, pp. 611–619.
5. Demirel, C. Experimentelle Untersuchung und Simulation des Abschreckprozesses von bauteilähnlichen Geometrien aus G-AlSi7Mg. 2009. Available online: https://depositonce.tu-berlin.de/items/a928e92c-4afe-4351-9012-e3b9ad23666b (accessed on 19 November 2024).
6. Donnelly, B.; O'Donovan, T.S.; Murray, D.B. Bubble Enhanced Heat Transfer from a Vertical Heated Surface. *J. Enhanc. Heat Transf.* **2008**, *15*, 159–169. [CrossRef]
7. Krause, F.; Schüttenberg, S.; Fritsching, U. Modelling and Simulation of Flow Boiling Heat Transfer. *Int. J. Numer. Methods Heat Fluid Flow* **2010**, *20*, 312–331. [CrossRef]
8. El Kosseifi, N. *Numerical Simulation of Boiling for Industrial Quenching Processes*; Ecole Nationale Supérieure des Mines de Paris: Paris, France, 2012.
9. John, V.; Kindl, A.; Suciu, C. Finite Element LES and VMS Methods on Tetrahedral Meshes. *J. Comput. Appl. Math.* **2010**, *233*, 3095–3102. [CrossRef]
10. Magnini, M. CFD Modeling of Two-Phase Boiling Flows in the Slug Flow Regime with an Interface Capturing Technique. Ph.D. Thesis, Alma Mater Studiorum—Università di Bologna, Bologna, Italy, 2012.
11. Landek, D.; Župan, J.; Filetin, T. A Prediction of Quenching Parameters Using Inverse Analysis. *Matls. Perf. Charact.* **2014**, *3*, 229–241. [CrossRef]
12. Tensi, H.M. Wetting Kinematics. In *Theory and Technology of Quenching: A Handbook*; Liščić, B., Tensi, H.M., Luty, W., Eds.; Springer: Berlin/Heidelberg, Germany, 1992; pp. 93–116, ISBN 978-3-662-01596-4.
13. Felde, I.; Shi, W. Hybrid Approach for Solution of Inverse Heat Conduction Problems. In Proceedings of the 2014 IEEE International Conference on Systems, Man, and Cybernetics (SMC), San Diego, CA, USA, 5–8 October 2014; IEEE: Piscataway, NJ, USA, 2014; pp. 3896–3899.
14. Steuer, R. *Ultraschallunterstütztes Flüssigkeitsabschrecken Bei Der Wärmebehandlung Metallischer Werkstoffe*; Forschungsberichte des Lehrstuhls für Werkstofftechnik der Universität Rostock; Shaker Verlag: Aachen, Germany, 2015; Volume 4, ISBN 978-3-8440-3667-1.
15. Subhash, M. Computational Modelling of Liquid Jet Impingement onto Heated Surface. Ph.D. Thesis, Technische Universität: Darmstadt, Darmstadt, Germany, 2017.
16. Bahbah, C. Méthodes Numériques Avancées Pour La Simulation Du Procédé de Trempe Industrielle. Ph.D. Thesis, Université Paris Sciences et Lettres, Paris, France, 2020.
17. Panda, A. Direct Numerical Simulations of Heat and Mass Transport in Multiphase Flows. Ph.D. Thesis, Technische Universiteit Eindhoven, Eindhoven, The Netherlands, 2020.
18. Ebrahim, S.A.; Cheung, F.-B.; Bajorek, S.M.; Tien, K.; Hoxie, C.L. Heat Transfer Correlation for Film Boiling during Quenching of Micro-Structured Surfaces. *Nucl. Eng. Des.* **2022**, *398*, 111943. [CrossRef]
19. Gamidi, K.; Pasam, V.K. Analysis of Residual Stresses in Spot Cooled Vibration Assisted Turning of Ti6Al4V Alloy Using Computational Fluid Dynamics-Aided Finite Element Method. *J. Mater. Eng. Perform.* **2024**, *33*, 3731–3745. [CrossRef]
20. Gupta, P.K.; Yadav, N.P. Numerical Investigation Into Convective Heat Transfer Coefficient of the Grinding Fluid Used in a Deep Grinding Process. *Trans. FAMENA* **2024**, *48*, 129–144. [CrossRef]
21. Hannoschöck, N. *Wärmeleitung und -transport: Grundlagen der Wärme- und Stoffübertragung*; Springer Berlin Heidelberg: Berlin/Heidelberg, Germany, 2018; ISBN 978-3-662-57571-0.
22. Bourouga, B.; Gilles, J. Roles of heat transfer modes on transient cooling by quenching process. *Int. J. Mater Form* **2009**, *3*, 77–88. [CrossRef]
23. Cukrov, A.; Sato, Y.; Boras, I.; Ničeno, B. A Solution to Stefan Problem Using Eulerian Two-Fluid VOF Model. *Brodogr. Int. J. Nav. Archit. Ocean. Eng. Res. Dev.* **2021**, *72*, 141–164. [CrossRef]
24. Cukrov, A.; Landek, D.; Sato, Y.; Boras, I.; Ničeno, B. Numerical simulation of film boiling heat transfer in immersion quenching process using Eulerian two-fluid approach. *Case Stud. Therm. Eng.* **2024**, *64*, 105497. [CrossRef]

25. Gauss, F.; Lucas, D.; Krepper, E. Grid Studies for the Simulation of Resolved Structures in an Eulerian Two-Fluid Framework. *Nucl. Eng. Des.* **2016**, *305*, 371–377. [CrossRef]
26. Liu, Y.; Pointer, W.D. *Eulerian Two-Fluid RANS-Based CFD Simulations of a Helical Coil Steam Generator Boiling Tube*; Oak Ridge National Lab. (ORNL): Oak Ridge, TN, USA, 2017.
27. Ansys® Fluent. *ANSYS Fluent Theory Guide, Release 19.2*; Help System; ANSYS, Inc.: Canonsburg, PA, USA, 2019.
28. Perić, M. Modeling of Free-Surface Flow With Focus on the VOF-Method. In Proceedings of the 17th Multiphase Flow Conference and Short Course, Helmholtz-Zentrum Dresden—Rossendorf, Dresden, Germany, 11–15 November 2019.
29. Drew, D.A.; Passman, S.L. *Theory of Multicomponent Fluids*; Springer Science & Business Media: Berlin/Heidelberg, Germany, 2006; Volume 135, ISBN 0-387-22637-0.
30. Höhne, T.; Vallée, C. Experiments and Numerical Simulations of Horizontal Two-Phase Flow Regimes Using an Interfacial Area Density Model. *J. Comput. Multiph. Flows* **2010**, *2*, 131–143. [CrossRef]
31. Denèfle, R.; Mimouni, S.; Caltagirone, J.-P.; Vincent, S. Multifield Hybrid Approach for Two-Phase Flow Modeling—Part 1: Adiabatic Flows. *Comput. Fluids* **2015**, *113*, 106–111. [CrossRef]
32. Kharangate, C.R.; Lee, H.; Mudawar, I. Computational Modeling of Turbulent Evaporating Falling Films. *Int. J. Heat Mass Transf.* **2015**, *81*, 52–62. [CrossRef]
33. Mer, S.; Praud, O.; Neau, H.; Merigoux, N.; Magnaudet, J.; Roig, V. The Emptying of a Bottle as a Test Case for Assessing Interfacial Momentum Exchange Models for Euler–Euler Simulations of Multi-Scale Gas-Liquid Flows. *Int. J. Multiph. Flow* **2018**, *106*, 109–124. [CrossRef]
34. Štrubelj, L.; Tiselj, I.; Mavko, B. Simulations of Free Surface Flows with Implementation of Surface Tension and Interface Sharpening in the Two-Fluid Model. *Int. J. Heat Fluid Flow* **2009**, *30*, 741–750. [CrossRef]
35. de Bertodano, M.L.; Fullmer, W.; Clausse, A.; Ransom, V.H. Introduction. In *Two-Fluid Model Stability, Simulation and Chaos*; de Bertodano, M.L., Fullmer, W., Clausse, A., Ransom, V.H., Eds.; Springer International Publishing: Cham, Switzerland, 2017; pp. 1–8, ISBN 978-3-319-44968-5.
36. Malikov, Z. Mathematical Model of Turbulence Based on the Dynamics of Two Fluids. *Appl. Math. Model.* **2020**, *82*, 409–436. [CrossRef]
37. Kharangate, C.R.; Mudawar, I. Review of Computational Studies on Boiling and Condensation. *Int. J. Heat Mass Transf.* **2017**, *108*, 1164–1196. [CrossRef]
38. Cukrov, A.; Sato, Y.; Boras, I.; Ničeno, B. Film Boiling around a Finite Size Cylindrical Specimen—A Transient Conjugate Heat Transfer Approach. *Appl. Sci.* **2023**, *13*, 9144. [CrossRef]
39. Hillier, A.; Doorsselaere, T.V.; Karampelas, K. Estimating the Energy Dissipation from Kelvin–Helmholtz Instability Induced Turbulence in Oscillating Coronal Loops. *ApJL* **2020**, *897*, L13. [CrossRef]
40. Yamada, T.; Shigechi, T.; Momoki, S.; Kanemaru, K. An Analysis of Film Boiling around a Vertical Finite-Length Cylinder. *Rep. Fac. Eng. Nagasaki Univ.* **2001**, *31*, 1–11.
41. Aubram, D. *An Arbitrary Lagrangian-Eulerian Method for Penetration into Sand at Finite Deformation*; Shaker: Düren, Germany, 2014; ISBN 978-3-8440-2507-1.
42. Cukrov, A.; Landek, D.; Sato, Y.; Boras, I.; Ničeno, B. Water Entry of a Heated Axisymmetric Vertical Cylinder. *Energies* **2023**, *16*, 7926. [CrossRef]
43. Dobrzynski, C. Adaptation de Maillage Anisotrope 3D et Application à l'aéro-Thermique Des bâtiments. Ph.D. Thesis, Université Pierre et Marie Curie—Paris VI, Paris, France, 2005.
44. Olivier, G. *Anisotropic Metric-Based Mesh Adaptation for Unsteady CFD Simulations Involving Moving Geometries, Adaptation de Maillage Anisotrope Par Prescription de Champ de Métriques Appliquée Aux Simulations Instationnaires En Géométrie Mobile*; Université Pierre et Marie Curie—Paris VI: Paris, France, 2011.
45. Barral, N. *Time-Accurate Anisotropic Mesh Adaptation for Three-Dimensional Moving Mesh Problems, Adaptation de Maillage Anisotrope Dépendant Du Temps Pour Des Problèmes Tridimensionnels En Maillage Mobile*; Université Pierre et Marie Curie—Paris VI: Paris, France, 2015.
46. MacKenzie, D.S. Understanding the Cooling Curve Test. *Therm. Process.* **2017**, 28–32. Available online: https://thermalprocessing.com/wp-content/uploads/2017/201701/0117-ASM.pdf (accessed on 19 November 2024).
47. Jagga, S.; Vanapalli, S. Cool-down Time of a Polypropylene Vial Quenched in Liquid Nitrogen. *Int. Commun. Heat Mass Transf.* **2020**, *118*, 104821. [CrossRef]
48. Mayinger, F. Blasenbildung und Wärmeübergang beim Sieden in freier und erzwungener Konvektion. *Chem. Ing. Tech.* **1975**, *47*, 737–748. [CrossRef]
49. Bucci, M.; Buongiorno, J.; Bucci, M. The Not-so-Subtle Flaws of the Force Balance Approach to Predict the Departure of Bubbles in Boiling Heat Transfer. *Phys. Fluids* **2021**, *33*, 017110. [CrossRef]

50. Cukrov, A.; Landek, D.; Sato, Y.; Boras, I.; Ničeno, B. The Development of Numerical Method for Simulation of Metal Materials Quenching. *Rud. Geol. Naft. Zb.* **2025**, *40. in press*.
51. Sato, Y.; Ničeno, B. Pool boiling simulation using an interface tracking method: From nucleate boiling to film boiling regime through critical heat flux. *Int. J. Heat Mass Transf.* **2018**, *125*, 876–890. [CrossRef]

**Disclaimer/Publisher's Note:** The statements, opinions and data contained in all publications are solely those of the individual author(s) and contributor(s) and not of MDPI and/or the editor(s). MDPI and/or the editor(s) disclaim responsibility for any injury to people or property resulting from any ideas, methods, instructions or products referred to in the content.